

---

# Discovery and Expansion of New Domains within Diffusion Models

---

Ye Zhu<sup>1</sup>, Yu Wu<sup>2</sup>, Duo Xu<sup>3</sup>, Zhiwei Deng<sup>4</sup>, Yan Yan<sup>5</sup>, Olga Russakovsky<sup>1</sup>

<sup>1</sup>Department of Computer Science, Princeton University

<sup>2</sup>School of Computer Science, Wuhan University

<sup>3</sup>Department of Astronomy, University of Virginia

<sup>4</sup>Google DeepMind

<sup>5</sup>Department of Computer Science, Illinois Institute of Technology

## Abstract

In this work, we study the generalization properties of diffusion models in a few-shot setup, introduce a novel tuning-free paradigm to synthesize the target out-of-domain (OOD) data, and demonstrate its advantages compared to existing methods in data-sparse scenarios with large domain gaps. Specifically, given a pre-trained model and a small set of images that are OOD relative to the model’s training distribution, we explore whether the *frozen* model is able to generalize to this new domain. We begin by revealing that Denoising Diffusion Probabilistic Models (DDPMs) trained on single-domain images are already equipped with sufficient representation abilities to reconstruct arbitrary images from the inverted latent encoding following bi-directional deterministic diffusion and denoising trajectories. We then demonstrate through both theoretical and empirical perspectives that the OOD images establish Gaussian priors in latent spaces of the given model, and the inverted latent modes are separable from their initial training domain. We then introduce our novel tuning-free paradigm to synthesize new images of the target unseen domain by *discovering* qualified OOD latent encodings in the inverted noisy spaces. This is *fundamentally different* from the current paradigm that seeks to modify the denoising trajectory to achieve the same goal by tuning the model parameters. Extensive cross-model and domain experiments show that our proposed method can expand the latent space and generate unseen images via frozen DDPMs without impairing the quality of generation of their original domain. We also showcase a practical application of our proposed heuristic approach in dramatically different domains using astrophysical data, revealing the great potential of such a generalization paradigm in data sparse fields such as scientific explorations.

## 1 Introduction

Generalization ability, which enables the model to synthesize data from various domains, has long been a challenge in deep generative models. The current research trend focuses on leveraging larger models with more training data to facilitate improved generalization. The popularity of recent large-scale models such as DALLÉ-2 [40], Imagen [20] and StableDiffusion [43] have demonstrated the impressive and promising representation abilities of the state-of-the-art (SOTA) diffusion generative models when trained on an enormous amount of images such as LAION-5B [44]. However, scaling up is not a panacea and does not fundamentally solve the generalization challenge. In other words, for data domains that remain sparse in those already giant datasets, such as the astrophysical observation and simulation data, even the SOTA models fail to synthesize data suitable for rigorous scientific research purposes, as illustrated in the middle columns of Fig. 1. In addition, scaling up requires exhaustive resources, severely limiting the number of research groups that are able to participate and

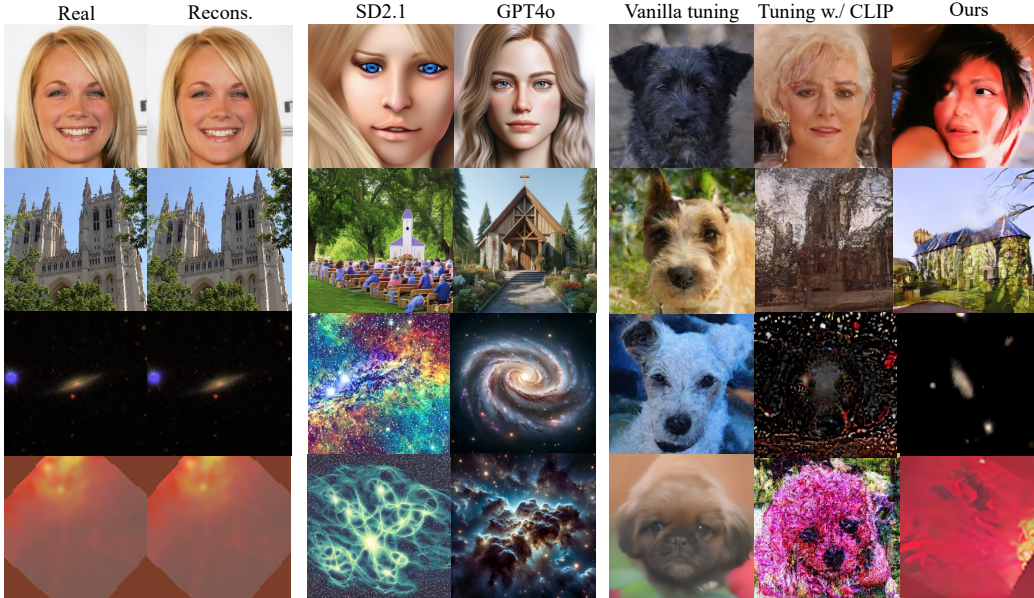


Figure 1: **Examples of synthesized OOD images across data domains and methods.** (*Left*): Using a pre-trained DDPM on dog images as an example, we can well reconstruct arbitrary unseen images across domains covering natural images and astrophysical data. (*Middle*): Even though large SOTA generative models have strong generalization abilities, their synthesized data are still very different from real data in specific domains. (*Right*): In this work, we propose a discovery-based tuning-free paradigm for synthesizing OOD data in a few-shot scenario. Different from tuning-based methods that usually yield better performance with closer domain gaps (e.g., dogs to humans), our method shows superiority as the domain gaps become larger.

contribute to the work, and consequently hindering research progress. Given the aforementioned concerns, our work focuses on studying the generalization ability in a few-shot setup, where a pre-trained diffusion generative model and a small set of raw images different from its training domain are provided, with the ultimate objective of generating new data samples from the target OOD domain.

Recall the generation process with a diffusion model (or most generative models in general), which essentially involves two steps: latent encoding sampling<sup>1</sup> and denoising.<sup>2</sup> In the realm of natural images within the computer vision community, most existing works address the problem by modifying trajectories and fine-tuning model parameters using new images and extra semantic supervision from the text [29, 67, 31]. However, tuning-based methods have several drawbacks, especially given the large transition gap between trained and target data domains. It is known that tuning methods *do not generalize well* when the domain gap between the target OOD domain and the training domain becomes too large [69, 70, 56]. In fact, our experiments show that tuning pre-trained DMs using only image supervisions with vanilla variational lower bound loss [19] is *very difficult*. Only with additional semantic guidance, such as CLIP loss [39], can tuning performance improve, as demonstrated in Fig. 1. Moreover, modifying parameters adversely affects synthesis quality in the model’s originally trained domain. The tuning cost is also entirely dependent on the pre-trained model, which can be quite high given the well-known expensive training for diffusion models. Unlike the existing trajectory-tuning paradigm, we introduce a heuristic approach featuring a novel *tuning-free* paradigm that achieves the objective by sampling latent encodings of the unseen target domain within the latent spaces of pre-trained diffusion models. Our core idea is to discover the corresponding OOD latent encodings and then denoise them through deterministic trajectories, as depicted in Fig. 2.

We begin with an in-depth study of the generalization properties of diffusion models. As a pivotal observation, we note that the SOTA diffusion generative models pre-trained on single-domain images

<sup>1</sup>The latent spaces in this work are different from the concept of LDMs (aka, StableDiffusion [43]), where the diffusion denoising operates on the latent space of raw data from autoencoders. Our latent spaces refer to intermediate noisy states along the denoising chain, similar to [74].

<sup>2</sup>The denoising can be considered as the trajectory mapping between the latent space and the real data space.

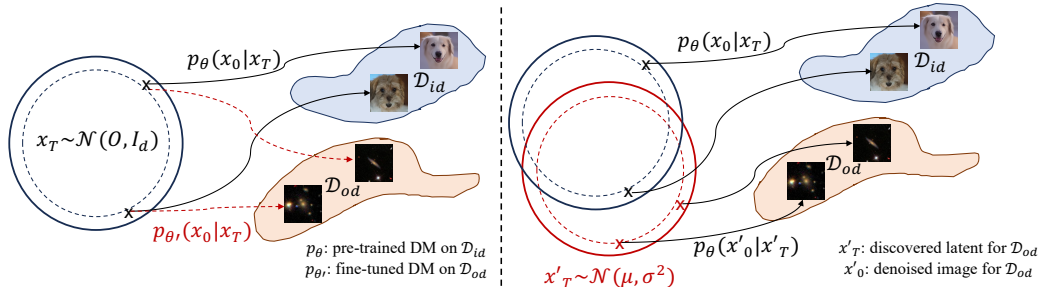


Figure 2: **Illustration of the trajectory-tuning based paradigm (left) and our proposed latent-discovery based paradigm (right) for OOD image synthesis with diffusion models.** Given a pre-trained DM  $p_{\theta}$  on images from domain  $\mathcal{D}_{id}$ , most existing methods seek to finetune the generation trajectories  $p_{\theta'}$  to synthesis data in a new domain  $\mathcal{D}_{od}$ . In contrast, we propose to discover unseen latent encodings to achieve the same goal via the frozen model  $p_{\theta}$  by expanding the latent spaces.

(e.g., dog faces) already have sufficient representation ability to reconstruct images from arbitrary unseen domains (e.g., human faces and churches) from the inverted OOD latent encodings,<sup>3</sup> as qualitatively shown in Fig. 1, and with details explained in Sec. 2.2. The results from the arbitrary image reconstruction test suggest that *an inverse direction* to solve our task objective: by *identifying additional qualified OOD latent encodings* based on the established priors from a limited set of OOD images, we can synthesize unseen images without the need to adjust the original model parameters. Specifically, we note that the reconstruction ability of unseen data is subject to the prerequisite of the deterministic inversion (i.e., diffusion direction) and denoising (i.e., reserve direction) trajectories [48], as described in Sec. 2.3. To better understand the generalization abilities of DDPMs, we provide a theoretically grounded explanation to show that the inverted OOD encodings establish *parameter-independent* Gaussian priors, as detailed in Sec. 2.4. Meanwhile, we explicitly formulate the “mode separability” problem within the context of diffusion models, and empirically verify that the inverted OOD latent encodings are distinguishable from those corresponding to the training domain to avoid the “mode interference” issue in Sec. 2.5, which is also qualitatively illustrated in Fig. 3.

The second contribution of this work introduces our paradigmatic design that achieves unseen domain synthesis in a tuning-free manner by discovering additional latent OOD encodings based on the inverted priors, as described in Sec. 3. Conceptually inspired by recent works that seek to manipulate the in-domain semantic attribute direction for data editing [74, 5], the key idea of our proposed OOD sampling method focuses on identifying potential latent directions by leveraging the geometric properties of the inverted OOD domains as additional domain-specific priors. The key takeaway from this part echoes our earlier analysis, demonstrating that in this latent discovery-based paradigm, the core technical challenge arises from the tendency of discovered OOD samples to be interfered with and captured by the original trained domain. This further underscores its distinguishable nature with intuitive tuning-based methods, where smaller data domain gaps are preferable for achieving better generalization performance.

As our last but not least contribution, we conduct extensive experiments in cross-model and cross-domain settings to demonstrate the effectiveness of our proposed paradigm, particularly its superiority in scenarios with large domain gaps between trained and target OOD data as detailed in Sec. 4. Notably, our experiments integrate both natural images (CelebA-HQ [26], AFHQ-Dog [8], LSUN-Church [65], LSUN-Bedroom [65]) and specific astrophysical data (GalaxyZoo [58] observation images and radiation field simulations of the dust emission [62]) to address a wide and representative range of domain gap differences. In addition to the quantitative and qualitative evaluation of natural images, widely adopted in the machine learning community, we also involve astrophysicists to assess the quality of generated data in comparison to their true astrophysical simulations. These comprehensive evaluations further reinforce our findings.

In summary, through the three contributions mentioned above, we aim to provide insights into a novel perspective for understanding and rethinking the domain generalization abilities of diffusion models, and to shed light on potential directions for broader interdisciplinary applications.

<sup>3</sup>Inversion refers to the process of converting raw data to noisy encodings in the literature of generative modeling [61], which can also be understood as a diffusion process in the context of DMs.

## 2 Domain Discovery and Expansion of DDPMs

This section presents the problem formulation of DDPMs [19] under the few-shot scenario and our analytical studies on the generalization properties of pre-trained DDPMs in the context of deterministic trajectories from both theoretical and empirical perspectives. The high-level takeaway from our in-depth study is that the inverted OOD samples establish Gaussian that is separable from the trained ID prior. The key technical challenge is to find qualified OOD latent free from the “*mode interference*”, which is distinguishable from the common understanding in tuning-based designs.

### 2.1 Problem Formulation

Given a DDPM  $p_\theta$  trained on images from a domain  $\mathcal{D}_{id}$ , we aim to investigate the generalization properties of  $p_\theta$  on other domain  $\mathcal{D}_{od}$  using  $N$  data samples  $\mathbf{x}_{od} \in \mathcal{D}_{od}$ , and eventually generate new data samples  $\mathbf{x}'_{od} \in \mathcal{D}_{od}$ .

The objective of DDPMs is similar to most previous generative models, which is to approximate an implicit data distribution  $q(\mathbf{x}_0)$  with a learned model distribution  $p_\theta(\mathbf{x}_0)$ , as well as providing an easy-to-sample proxy (e.g., standard Gaussian). We further use  $p_s$  and  $p_i$  to represent the stochastic [19] and deterministic [48] generation processes, respectively. For the opposite direction, the pre-defined diffusion procedure is often denoted by  $q(\mathbf{x}_{1:T}|q_0)$ . In addition, we use the hyper-parameter  $\eta$  [48] to characterize the degree of stochasticity in the generative process, with  $\eta = 1$  for  $p_s$  and  $\eta = 0$  for  $p_i$ . At intermediate stochastic levels, we adopt the notation  $p_{\eta=k}$  with  $k$  equals a constant between 0 and 1. Similar to existing literature,  $T$  denotes the total diffusion steps. We use  $\mathcal{X}_t$  to represent the latent (noisy) spaces formed by  $\mathbf{x}_t$  along denoising.

### 2.2 Representation Ability of Latent Spaces

We observe that a DDPM, trained even on a single-domain small dataset (e.g., dog faces), already has sufficient representation ability to accurately reconstruct arbitrary unseen images (e.g., human, church, and astrophysical data), as shown in the second column of Fig. 1. The reconstruction ability is subject to the deterministic inversion and denoising trajectories [48], which can be considered as a special case of vanilla stochastic process [19] as detailed in Sec. 2.3. The findings above suggest that: with a good mapping approximator (i.e., pre-trained DDPM) and proper tool (i.e., deterministic trajectories with DDIMs), its intermediate latent spaces already have sufficient representation ability for arbitrary images, which opens up the possibility to leverage DDPMs for synthesizing images from new domains *without tuning* the model parameters. The quantitative evaluation of the reconstruction results is in Tab. 3 in the Appendices.

### 2.3 Deterministic Diffusion Models

The core idea in the context of deterministic non-Markovian DDIMs [48] is to consider a family of  $\mathcal{Q}$  of inference distributions, indexed by a real vector  $\sigma \in \mathbb{R}_{\geq 0}^T$ :

$$q_\sigma(\mathbf{x}_{1:T}|\mathbf{x}_0) := q_\sigma(\mathbf{x}_T|\mathbf{x}_0) \prod_{t=2}^T q_\sigma(\mathbf{x}_{t-1}|\mathbf{x}_t, \mathbf{x}_0), \quad (1)$$

where  $q_\sigma(\mathbf{x}_T|\mathbf{x}_0) = \mathcal{N}(\sqrt{\alpha_T}\mathbf{x}_0, (1 - \alpha_T)\mathbf{I})$  and  $\forall t > 1$ ,

$$q_\sigma(\mathbf{x}_{t-1}|\mathbf{x}_t, \mathbf{x}_0) = \mathcal{N}(\sqrt{\alpha_{t-1}}\mathbf{x}_0 + \sqrt{1 - \alpha_{t-1} - \sigma_t^2} \cdot \frac{\mathbf{x}_t - \sqrt{\alpha_t}\mathbf{x}_0}{\sqrt{1 - \alpha_t}}, \sigma_t^2\mathbf{I}), \quad (2)$$

with  $\alpha_{1:T} \in (0, 1]^T$  is a decreasing sequence that parameterizes Gaussian transition kernels.

While this deterministic line of works was initially proposed to accelerate the vanilla ancestral sampling, later studies [31, 74, 64] revealed that the deterministic diffusion can be used as a tractable and lossless way for conducting data inversion, by connecting the above Eqn. 2 to neural ODEs. Similar deterministic variant is also proposed for the score-based formulations [51]. In this work, we leverage the deterministic properties as the tool for inversion and denoising the unseen images. More details about the deterministic inversion and denoising methods are included in Appendix C.

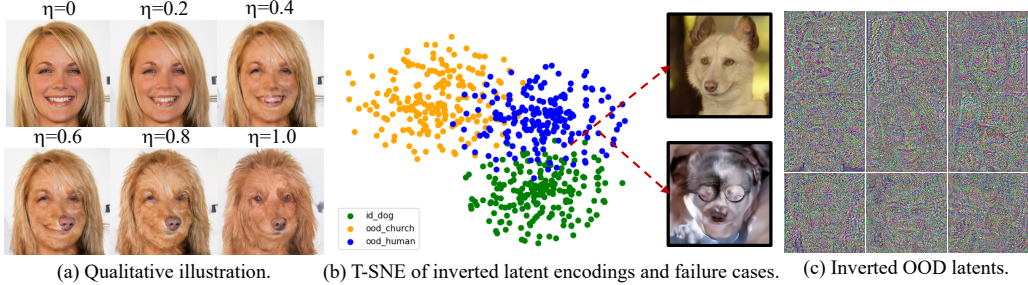


Figure 3: **Various visualizations of “mode interference”**. Given an example setting of synthesizing human faces from DDPMs trained on dogs. (a): An interfered image of human faces gradually becomes similar to its original trained domain as the denoising trajectory shifts from deterministic ( $\eta = 0$ ) to stochastic ( $\eta = 1$ ). (b): Failure cases happen when sampled latent OOD encodings are captured by the model’s original probabilistic concentration mass. (c): Inverted OOD latent encodings preserve slight perceptible low-level visual features and are not *perfect* Gaussians but rather approximations.

## 2.4 Parameter-Independent Properties: Gaussian Priors

We seek a theoretically grounded explanation to the generalization properties of pre-trained DDPMs after the inversion. The takeaway message is: *In theory*, the inverted latent encodings also establish Gaussian priors as presented in Lemma 2.1.<sup>4</sup>

**Lemma 2.1.** For  $q_\sigma(\mathbf{x}_{1:T}|\mathbf{x}_0)$  defined in Eqn. 1 and  $q_\sigma(\mathbf{x}_{t-1}|\mathbf{x}_t, \mathbf{x}_0)$  defined in Eqn. 2, we have:

$$q_\sigma(\mathbf{x}_t|\mathbf{x}_0) = \mathcal{N}(\sqrt{\alpha_t}\mathbf{x}_0, (1 - \alpha_t)\mathbf{I}). \quad (3)$$

As also mentioned in [48], one can derive Lemma 2.1 by assuming for any  $t \leq T$ ,  $q_\sigma(\mathbf{x}_t|\mathbf{x}_0) = \mathcal{N}(\sqrt{\alpha_t}\mathbf{x}_0, (1 - \alpha_t)\mathbf{I})$  holds, if:

$$q_\sigma(\mathbf{x}_{t-1}|\mathbf{x}_0) = \mathcal{N}(\sqrt{\alpha_{t-1}}\mathbf{x}_0, (1 - \alpha_{t-1})\mathbf{I}), \quad (4)$$

and then prove the statement with an induction argument for  $t$  from  $T$  to 1, since the base case ( $t = T$ ) already holds by definition. Proof details can be found in Appendix D, and we note that derivations are completed in the forward diffusion direction (i.e., the inversion direction from data to latent spaces), and make no modification to the trained model. This sets the *primary rationale* for estimating the latent distributions as Gaussian in a model parameter-independent manner.

## 2.5 Data-Dependent Properties: Mode Interference and Separability

In the literature of GANs-based generative models [15], “mode collapse” is a common issue that describes the training failure when generated images tend to be very similar given randomly sampled starting encodings from the Gaussian prior. Within the context of diffusion models in our work, we explicitly reveal a phenomenon analog to the “mode collapse” in GANs, which we refer to as “*mode interference*”, as qualitatively illustrated in Fig. 3 (a).

Intuitively, “*mode interference*” describes the case when the denoised images fall into the model’s original training domain  $\mathcal{D}_{id}$  instead of the target unseen domain  $\mathcal{D}_{od}$  due to the prior interference in the latent spaces. Specifically, when we sample directly from the standard Gaussian to obtain a latent encoding  $\mathbf{x}_T \sim \mathcal{N}(\mathbf{0}, \mathbf{I}_d)$ , then the denoised image will surely fall into the original training domain  $\mathbf{x}_0 \in \mathcal{D}_{id}$  with  $\mathbf{x}_0 \sim p_\theta(\mathbf{x}_0)$ , which is the vanilla generation process of a trained DDPM. However, it contradicts our task objective to synthesize images  $\mathbf{x}'_0 \in \mathcal{D}_{od}$ . As illustrated in Fig. 2, since we are denoising the latent encoding via deterministic trajectories  $p_i$ , the remaining critical technical challenge to generate  $\mathbf{x}'_0$  is to find additional qualified latent encoding  $\mathbf{x}'_T$  *free from the interference* of the ID Gaussian mode in the sampling stage.

Notably, a key precondition to achieving the effective OOD latent sampling is that the established OOD prior mode *should be separable* from the ID Gaussian prior mode (i.e., a standard Gaussian). Otherwise, the denoised image would fall into the training domain as in Fig. 3 (b). The separability is further supported and validated by our empirical verification below in Sec. 2.6.

<sup>4</sup>However, in practice, due to the fact that pre-trained DMs themselves are function approximators, the samples after inversion do not establish perfect Gaussians but rather approximations, echoing Sec. 3.



Table 1: **Geometric properties of inverted ID and OOD latent encodings.** The results are computed based on 1K sample pairs. We report the mean and std for each geometric measurement to ensure the statistical significance. The base model is trained on AFHQ-Dog [8] in 256x256.

$\mathcal{D}$	Dog (ID)	Human (O)	Bedroom (O)	Church (O)	Astro. Galaxy (O)	Astro. Turbulence (O)
Pair-Angle	60.0±0	60.0±0	60.0±0.1	60.0±0.1	60.0±0.1	60.0 ± 0
Angle-Origin	89.7±0.01	89.7±0	89.8±0.01	89.7±0.01	89.1±0.01	87.6 ±0.03
Pair-Distance	607.4±0.01	611.4±0.05	611.2±0.07	609.9±0.02	612.37±0.05	609.13 ± 0.1
Center-Distance	-	33.3	26.0	33.2	54.7	60.8
Clf. Acc.	-	0.97	0.99	0.99	1.0	1.0

## 2.6 Analytical Experiments

We show empirical verification from multiple perspectives to support our parameter-independent and data-dependent properties described in Sec. 2.4 and Sec. 2.5.

**Geometrical Properties of Gaussians.** We leverage the geometrical measurements established of the high-dimensional studies in mathematics [7], as additional empirical support for the Gaussian priors in Sec. 2.4. Specifically, we compute several geometric metrics, including the pair-wise angles (angles formed by three arbitrary samples), sample-to-origin angles (angles formed by two arbitrary samples and the origin), pair-wise distance (euclidean distance between two arbitrary samples) and distance between OOD and ID Gaussian centers, and list the results in Tab. 1.

Characteristics above are typical geometric properties possessed by isotropic high-dimensional Gaussians [7]. Notably, three randomly sampled points from a high-dimensional Gaussian are almost surely form an equilateral triangle and are almost surely nearly orthogonal, which corresponds to the constant  $60^\circ$  pair-wise angle and  $90^\circ$  sample-to-origin angle in the first and second rows of Tab. 1, respectively. More details about the geometric properties are in Appendix D.

**Mode Separability.** As revealed by our analysis in Sec. 2.5, the separability between ID and OOD Gaussian modes is critical for synthesizing target unseen domain images without modifying the model parameters and for avoiding the “mode interference”. We further provide validation from the statistical and learning-based classifier perspectives to support the separability claim.

*Statistical Validation.* The separability of high-dimensional Gaussians follows Lemma 2.2 [7], which states that spherical Gaussians can be relaxingly separated by  $\Omega(d^{\frac{1}{4}})$ , or even  $\Omega(1)$  with more sophisticated algorithms. In other words, for a DDPM trained on  $256 \times 256$  images with dimensionality  $d = 3 \times 256 \times 256$ , ID and OOD modes can be well separated and avoid interference given a distance larger than  $d^{\frac{1}{4}} \approx 21$ , which is further validated by the empirical distance between centers, listed in the forth row of Tab. 1. More details about Lemma 2.2 are in Appendix D.

**Lemma 2.2.** *Mixtures of spherical Gaussians in  $d$  dimensions can be separated provided their centers are separated by more than  $d^{\frac{1}{4}}$  distance (i.e., a separation of  $\Omega(d^{\frac{1}{4}})$ ).*

*Classifier Validation.* Another empirical perspective to validate the separability between modes in the latent spaces is using the classifiers as in existing literature [45, 74]. Specifically, a linear classifier such as SVMs [17] can be fitted to test the separability between ID and OOD encodings in the latent spaces. In our analytical experiments, we fit SVMs on 1K inverted ID and OOD samples following the 7:3 training-testing ratio, and report the test accuracy in Tab. 1. As additional clarification, the classification results are obtained with the test on the latent space  $\mathcal{X}_T$ . Our rationale behind the choice of  $T$  corresponds to the recent findings of DMs [74, 64], which indicates that  $\mathcal{X}_T$ , as the departure latent space, has the largest probabilistic support for the trained domain. In other words, if the latent ID and OOD modes can be separated in  $\mathcal{X}_T$ , they can be separated more easily in other  $\mathcal{X}_t$ , for  $t = \{T - 1, \dots, t, \dots, 1\}$ .

As shown in Tab. 1, while performing the binary classification task on the inverted ID and OOD latent encodings, a simple linear classifier can well separate different domains, which further validates the latent modes are separable. In addition, we also observe that while the unseen images (e.g., human faces) are visually more similar to the trained domains (e.g., dogs), the inverted latent encodings *inherit such similarity*, making those unseen domains *more difficult to be separated* from the trained mode, and subsequently cause extra generation difficulties for those target domains via our tuning-free paradigm (see Sec. 3). We note this is distinguishable from previous tuning-based generalization works [69, 70, 56], which believe that it is usually easier to generalize model abilities to unseen domains similar to the trained ones, further validated in Sec. 4.

Our findings on the OOD mode separability also align with another thread of recent works that investigate pre-trained DDMs for discriminative tasks like classification and segmentation [32, 9, 38], where they reveal that diffusion models *generalize better to classifying out-of-distribution images*.

### 3 Discovery-based OOD Synthesis

Following our extensive analysis, we note that the methodological challenges in this work can be disentangled into two key points: sample qualified latent encodings from the OOD prior, and avoid the mode interference. Sampling from the inverted high-dimensional OOD priors, however, is an open and non-trivial challenging task given the theory-practice gap,<sup>5</sup> and points to multiple possible directions of solutions such as classic statistical techniques. In fact, high-dimensional Gaussian estimation itself remains a challenging and complex research topic, especially in a multi-variant case [71, 4]. While we present our proposed latent sampling method below, we have experimented with *many other methods* that may not yield the best performance, such as vanilla Gaussian sampling and MCMC, with detailed discussions in Appendix E.

**Few-Shot Latent References.** Having obtained  $\mathbf{x}_{od,t}$  from  $N$  raw images  $\mathbf{x}_{od}$ , it seems intuitive to directly sample from the estimated Gaussian  $\mathcal{N}(\mu_{est}, \sigma_{est}^2)$  from those inverted OOD latent encodings. However, we note this is insufficient to avoid the mode interference due to the fact that the empirical inversion does not establish perfect Gaussian *in practice* despite the theoretical Gaussian groundings, even for trained in-domain cases [74]. This is also qualitatively demonstrated in Fig. 3(c), where the inverted latent encodings preserve slight perceptible low-level visual features. To set a rather precise starting point in the OOD latent space, we thus propose to adopt the inverted samples  $\mathbf{x}_{od,t}$  as the starting point to navigate the following sampling process.

**Latent Direction for New Samples.** While the inverted latent sample  $\mathbf{x}_{od,t}$  serves as a known starting point, we continue to mine more unknown latent samples that shall lead to new denoised images  $\mathbf{x}'_{od}$ . Specifically, inspired by several recent works in image editing through latent direction guidance [74, 5], we deploy the samples  $\bar{\mathbf{x}}_{od,t} \sim \mathcal{N}(\mu_{est}, \sigma_{est}^2)$  drawn from the estimate Gaussian as the ultimate latent directions, and obtain samples  $x'_{od,t}$  along the spherical interpolation (slerp) [46] between  $\mathbf{x}_{od,t}$  and  $\bar{\mathbf{x}}_{od,t}$ . The rationale behind the spherical interpolation comes from the fact that the probabilistic concentration mass of a high-dimensional Gaussian is mainly centered around a thin annulus around the equator [7]. In the meantime, it is critical for discovered latent samples to stay within the area of high probabilistic concentration mass to ensure denoised data with high quality.

**Geometrical Optimization.** So far we have localized a trajectory with intermediate samples  $\mathbf{x}'_{od,t} \in \text{Slerp}(\mathbf{x}_{od,t}, \bar{\mathbf{x}}_{od,t})$  connecting two samples  $\mathbf{x}_{od,t}$  and  $\bar{\mathbf{x}}_{od,t}$  in this latent OOD space. To further improve the quality of our discovered latent samples, we leverage the geometric properties as domain-specific information to optimize the latent samples we have obtained from the previous step as additional criteria to avoid mode interference. Specifically, we can filter and reject a fraction of initial samples via the angles and distances as shown in Tab. 1 by setting pre-defined tolerance ranges  $\omega$ .

**Overall Algorithm.** The overall pipeline of our proposed OOD sampling method includes the following major steps: raw image inversion via  $p_i$ , geometric property computation (optional), latent sampling, and deterministic denoising via  $p_i$ . Details are depicted in Algo. 1 and 2 in Appendix E.

## 4 Generation Experiments

### 4.1 Experimental Setup

**Model Zoos and Datasets.** We adopt four pre-trained DDPMs on different single domain datasets as our base models for experiments: improved DDPM [36] trained on AFHQ-Dog [8], and DDPM [19] trained on CelebA-HQ [26], LSUN-Church [65], and LSUN-Bedroom [65]. Each model generates images in the original resolution of  $256 \times 256$ , resulting in a total dimensionality of the latent spaces  $d = 256 \times 256 \times 3 = 196,608$ .

In addition to the above commonly used natural image datasets, we further experiment with two astrophysical datasets to cover a wide range of domain differences and to showcase the application

<sup>5</sup>As all the generative models can be considered as function approximators between the sampling prior and the implicit data distributions with certain error levels.

Table 2: **General quality evaluation in cross model and domain setup.**  $T$  stands for *Tuning-based*, and  $TF$  denotes *Tuning-Free*. We report the FID scores ( $\downarrow$ ) for natural image domains and the Mean Opinion Scores (MOS) ( $\uparrow$ ) from subjective evaluations with astrophysicists. Note that most baseline methods perform the *image-to-image translation* and use *additional CLIP loss* to tune the model, and thus largely facilitate the task by bypassing the actual sampling stage and with extra strong semantic guidance. We therefore call for special attention when comparing the scores for a comprehensive and objective assessment, qualitative examples in Fig. 1 and more samples in Appendix F.

Methods	Category	Dog	CelebA	Church	Bedroom	Galaxy	Radiation
Vanilla tuning	$T$	213.6 $\pm$ 4.8	229.7 $\pm$ 4.3	192.5 $\pm$ 3.7	191.1 $\pm$ 4.0	-	-
DiffusionCLIP [29]	$T$	73.6 $\pm$ 2.9	63.6 $\pm$ 3.0	66.3 $\pm$ 2.8	68.1 $\pm$ 2.8	-	-
Asyrp [31]	$T$	<b>66.4<math>\pm</math>2.1</b>	<b>58.7<math>\pm</math>2.4</b>	<b>62.5<math>\pm</math>2.0</b>	63.2 $\pm$ 1.9	1.84 $\pm$ 0.97	1.35 $\pm$ 0.74
Ours	$TF$	78.2 $\pm$ 2.8	64.5 $\pm$ 2.7	64.8 $\pm$ 2.7	<b>62.9<math>\pm</math>2.6</b>	<b>2.88<math>\pm</math>0.93</b>	<b>1.52<math>\pm</math>0.80</b>

scenarios with scientific data. Specifically, we adopt the GalaxyZoo [58] and the radiation simulation data [62], the latter has been investigated using DMs for prediction purposes. Details about those astrophysical datasets, their scientific interpretations, and evaluations are included in the Appendix F for interested readers, which differs from the usual interpretation of natural images.

**Comparisons.** Our main experiments focus on the comparison with the trajectory tuning-based approaches using the given DMs and OOD samples. Specially, we compare with vanilla tuning, where we finetune the pre-trained model with classic VLB loss [19] on unseen images, as well as several different SOTA image-to-image translation methods via diffusion models as baselines, as they also output images in domains that are different to the trained ones. However, it is worth noting that those baseline methods (*i.e.*, DiffusionClip [29], and Asyrp [31]) are *not really generating* unseen images, but rather *editing an given original ID image* to a target unseen domain. Moreover, those are learning-based methods trained on each unseen domain with extra CLIP loss [39], while our method operates on a single mutual latent space from the pre-trained base diffusion models *without* additional external supervision, echoing our conceptual design of “space expansion”.

**Implementations and Learning Budget.** We use  $N = 1000$  images for OOD domains. For deterministic diffusion, we adopt the standard DDIMs skipping step technique to accelerate both processes using 60 steps in total. Each direction takes an average of 3 - 6 seconds. We use the univariant Gaussian estimation for inverted OOD latent encodings. The geometric optimization tolerance  $\omega$  is set to be 0.3 for distance for 0.1 for angles, which leads to a rejection rate of approximately 84.44 % based on initial samples. We use 2 RTX 3090 GPUs for all experiments including baselines. For baseline methods that perform image translation and editing [29, 31], we use their respective officially released implementations, each tuning process takes approximately 30 mins, with an initial default learning rate of 2e-6. To ensure a fair comparison, we also stop the vanilla tuning after around 30 minutes, resulting in around 20 epochs of finetuning, with an even larger learning rate of 1e-5. For our proposed method, the inversion takes the same time as those baseline methods, but the core proposed sampling methods take *negligible time*.

## 4.2 Results, Evaluations, and Analysis

**General Quality.** As a general quality evaluation, we calculate the FID scores [18] on 5K generated samples for natural images and report the Mean Opinion Scores (MOS) for astrophysical data. The FID scores are averaged over four DDPMs pre-trained on different image domains, and the Mean Opinion Scores (MOS) with a scale between 1-5 are collected from subjective evaluations performed by astrophysicists with respect to the ground truth observation and simulation data in a *non cherry-picky manner*. As shown in Fig. 1 and Tab. 2, *vanilla tuning* with only image supervisions can *hardly* alter the original generation trajectories and synthesize desired images, always synthesizing in-domain images after comparable tuning time with other tuning baselines. As for methods that finetune the model with additional CLIP loss [39], such as DiffusionCLIP [29] and Asyrp [31], they relatively perform better for domains closer to their trained domains as expected. Our proposed method shows an opposite trend by achieving better performance in data domains with bigger differences, as it is easier to avoid mode interference with larger domain gaps in the latent spaces.

**Data Diversity.** The trade-off between the “general quality” and “diversity” of the synthesized data has long been a dilemma in the generative modeling study, as one can always trade one for another. *For natural image generation*, data diversity is a popular evaluation criteria; *for scientific data synthesis*, however, the embedded physical proper-



ties, rather than *the perceptual difference*, are usually more appreciated. As our proposed data sampling method in Sec. 3 deploys one inverted latent encoding  $\mathbf{x}_{od,t}$  as a reference before exploring new samples, one may be concerned that the synthesized data will look similar to the reference image after denoising. To address the above concern, we qualitatively show examples of the reference and sampled data after denoising for both ID and OOD cases in Fig. 4. We observe that, when applied in an ID scenario, our proposed tuning-free method can also synthesize data with sufficient diversity. The diversity is relatively reduced in closer natural image domains, but it becomes easier to synthesize more diverse data with larger domain gaps, consistent with the trend observed in general quality assessments. We also note that for tuning baselines with extra CLIP supervisions [29, 31], the data diversity is not explicitly used as an evaluation criterion given their task objective of data editing. On the contrary, the data after editing (is expected to) preserve very high similarity in visual appearance, but with only difference in semantic attribute.

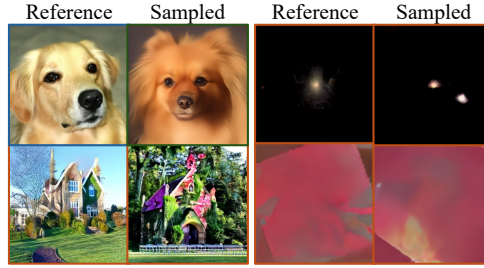


Figure 4: **Illustration of the data diversity between the latent reference and sampled data.** Dogs belong to the ID case, while the remaining ones are OODs.

**Impact of the Latent Step  $t$ .** We test the latent step  $t$  of diffusion models where we perform the latent inversion and OOD sampling as part of the ablation studies. As an overall takeaway, the choice of  $t$  also characterizes a *trade-off* between the sampling difficulty and the risk of “mode interference”. In other words, when  $t$  gets closer to the departure latent space  $\mathcal{X}_T$ , it is usually easier to conduct initial sampling as the inverted prior is closer to theoretical Gaussian but also tends to get more easily captured by the original trained domain as the ID latent spaces get larger probabilistic support in  $\mathcal{X}_T$ . Due to the space limit, we present other ablation studies that discuss the impact of the DDPM model designs and the degree of stochasticity in Appendix F.

## 5 Related Work

This work is closely related to several research fields such as the *generalization ability of generative models* [54, 43], the *diffusion models and their deterministic variants* [47, 49, 48, 51], the study on the *latent space of deep generative models* [26, 1, 12, 74], as well as recent downstream applications that use diffusion models for scientific explorations in a data-rare cases [62, 63]. Our work adopts a few-shot scenario to study the generalization abilities, uses the deterministic variant as the tool to achieve a bidirectional transition between latent noisy and data spaces, and contributes to a better understanding of those latent spaces. An extended discussion on related work is in Appendix B.

## 6 Further Discussions

**Conclusion.** To sum up, we study the generalization abilities of DDPMs in the few-shot scenario. From the analytical point of view, we explore the generalization properties of DDPMs on unseen OOD domains. From the methodological perspective, our analytical results allow us to propose a novel paradigm for synthesizing images from new domains without tuning the generative trajectories. We also showcase the superiority of our method in data-sparse cases with large domain gaps.

**Limitations and Future Directions.** The current limitations and challenge mainly come from the OOD sampling. As previously discussed, the sampling from inverted OOD prior in high dimensionality is a challenging task and open research question, which also directly impact the synthesized image quality. Improved sampling methods are worth investigating as future research directions.

**Broader Impact.** This work falls into the category of generative models and their applications, we thus acknowledge that it may pose the same risks of malicious use of synthetic data as other general generative works. We impose necessary safeguards to ensure the responsible usage and distribution of data. However, the primary objective of our work is not performance-driven but to provide a better understanding of the generalization properties of diffusion generative models.

## References

- [1] Rameen Abdal, Yipeng Qin, and Peter Wonka. Image2stylegan: How to embed images into the stylegan latent space? In *ICCV*, 2019.
- [2] Rameen Abdal, Yipeng Qin, and Peter Wonka. Image2stylegan++: How to edit the embedded images? In *CVPR*, 2020.
- [3] Yuval Alaluf, Or Patashnik, and Daniel Cohen-Or. Restyle: A residual-based stylegan encoder via iterative refinement. In *ICCV*, 2021.
- [4] Jushan Bai and Shuzhong Shi. Estimating high dimensional covariance matrices and its applications. 2011.
- [5] Stefan Andreas Baumann, Felix Krause, Michael Neumayr, Nick Stracke, Vincent Tao Hu, and Björn Ommer. Continuous, subject-specific attribute control in t2i models by identifying semantic directions. *arXiv preprint arXiv:2403.17064*, 2024.
- [6] Christopher M Bishop and Nasser M Nasrabadi. *Pattern recognition and machine learning*. Springer, 2006.
- [7] Avrim Blum, John Hopcroft, and Ravindran Kannan. *Foundations of data science*. Cambridge University Press, 2020.
- [8] Yunjey Choi, Youngjung Uh, Jaejun Yoo, and Jung-Woo Ha. Stargan v2: Diverse image synthesis for multiple domains. In *CVPR*, 2020.
- [9] Kevin Clark and Priyank Jaini. Text-to-image diffusion models are zero-shot classifiers. *NeurIPS*, 2023.
- [10] Antonia Creswell and Anil Anthony Bharath. Inverting the generator of a generative adversarial network. *IEEE TNNLS*, 2018.
- [11] Prafulla Dhariwal and Alexander Nichol. Diffusion models beat gans on image synthesis. In *NeurIPS*, 2021.
- [12] Rinon Gal, Or Patashnik, Haggai Maron, Amit H Bermano, Gal Chechik, and Daniel Cohen-Or. Stylegan-nada: Clip-guided domain adaptation of image generators. *ACM Transactions on Graphics (TOG)*, 41(4): 1–13, 2022.
- [13] Yaroslav Ganin, Evgeniya Ustinova, Hana Ajakan, Pascal Germain, Hugo Larochelle, François Laviolette, Mario Marchand, and Victor Lempitsky. Domain-adversarial training of neural networks. *The journal of machine learning research*, 2016.
- [14] Rui Gong, Wen Li, Yuhua Chen, and Luc Van Gool. Dlow: Domain flow for adaptation and generalization. In *CVPR*, 2019.
- [15] Ian Goodfellow, Jean Pouget-Abadie, Mehdi Mirza, Bing Xu, David Warde-Farley, Sherjil Ozair, Aaron Courville, and Yoshua Bengio. Generative adversarial nets. In *NeurIPS*, 2014.
- [16] Shuyang Gu, Dong Chen, Jianmin Bao, Fang Wen, Bo Zhang, Dongdong Chen, Lu Yuan, and Baining Guo. Vector quantized diffusion model for text-to-image synthesis. In *CVPR*, 2022.
- [17] Marti A. Hearst, Susan T Dumais, Edgar Osuna, John Platt, and Bernhard Scholkopf. Support vector machines. *IEEE Intelligent Systems and their applications*, 1998.
- [18] Martin Heusel, Hubert Ramsauer, Thomas Unterthiner, Bernhard Nessler, and Sepp Hochreiter. Gans trained by a two time-scale update rule converge to a local nash equilibrium. *NeurIPS*, 2017.
- [19] Jonathan Ho, Ajay Jain, and Pieter Abbeel. Denoising diffusion probabilistic models. In *NeurIPS*, 2020.
- [20] Jonathan Ho, William Chan, Chitwan Saharia, Jay Whang, Ruiqi Gao, Alexey Gritsenko, Diederik P Kingma, Ben Poole, Mohammad Norouzi, David J Fleet, et al. Imagen video: High definition video generation with diffusion models. *arXiv preprint arXiv:2210.02303*, 2022.
- [21] Jonathan Ho, Tim Salimans, Alexey Gritsenko, William Chan, Mohammad Norouzi, and David J Fleet. Video diffusion models. *NeurIPS Workshop*, 2022.
- [22] Judy Hoffman, Eric Tzeng, Taesung Park, Jun-Yan Zhu, Phillip Isola, Kate Saenko, Alexei Efros, and Trevor Darrell. Cycada: Cycle-consistent adversarial domain adaptation. In *ICML*. Pmlr, 2018.

- [23] Minghui Hu, Yujie Wang, Tat-Jen Cham, Jianfei Yang, and PN Suganthan. Global context with discrete diffusion in vector quantised modelling for image generation. *arXiv preprint arXiv:2112.01799*, 2021.
- [24] Minyoung Huh, Richard Zhang, Jun-Yan Zhu, Sylvain Paris, and Aaron Hertzmann. Transforming and projecting images into class-conditional generative networks. In *ECCV*. Springer, 2020.
- [25] Richard Arnold Johnson, Dean W Wichern, et al. Applied multivariate statistical analysis. 2002.
- [26] Tero Karras, Timo Aila, Samuli Laine, and Jaakko Lehtinen. Progressive growing of gans for improved quality, stability, and variation. *arXiv preprint arXiv:1710.10196*, 2017.
- [27] Tero Karras, Miika Aittala, Timo Aila, and Samuli Laine. Elucidating the design space of diffusion-based generative models. *arXiv preprint arXiv:2206.00364*, 2022.
- [28] Amirhossein Kazerouni, Ehsan Khodapanah Aghdam, Moein Heidari, Reza Azad, Mohsen Fayyaz, Ilker Hacihaliloglu, and Dorit Merhof. Diffusion models in medical imaging: A comprehensive survey. *Medical Image Analysis*, page 102846, 2023.
- [29] Gwanghyun Kim, Taesung Kwon, and Jong Chul Ye. Diffusionclip: Text-guided diffusion models for robust image manipulation. In *CVPR*, 2022.
- [30] Zhifeng Kong, Wei Ping, Jiaji Huang, Kexin Zhao, and Bryan Catanzaro. Diffwave: A versatile diffusion model for audio synthesis. In *ICLR*, 2020.
- [31] Mingi Kwon, Jaeseok Jeong, and Youngjung Uh. Diffusion models already have a semantic latent space. In *ICLR*, 2023.
- [32] Alexander C. Li, Mihir Prabhudesai, Shivam Duggal, Ellis Brown, and Deepak Pathak. Your diffusion model is secretly a zero-shot classifier. In *Proceedings of the IEEE/CVF International Conference on Computer Vision (ICCV)*, 2023.
- [33] Da Li, Yongxin Yang, Yi-Zhe Song, and Timothy M Hospedales. Deeper, broader and artier domain generalization. In *ICCV*, 2017.
- [34] Gautam Mittal, Jesse Engel, Curtis Hawthorne, and Ian Simon. Symbolic music generation with diffusion models. *arXiv preprint arXiv:2103.16091*, 2021.
- [35] Krikamol Muandet, David Balduzzi, and Bernhard Schölkopf. Domain generalization via invariant feature representation. In *ICML*. PMLR, 2013.
- [36] Alexander Quinn Nichol and Prafulla Dhariwal. Improved denoising diffusion probabilistic models. In *ICML*. PMLR, 2021.
- [37] Xingchao Peng, Qinxun Bai, Xide Xia, Zijun Huang, Kate Saenko, and Bo Wang. Moment matching for multi-source domain adaptation. In *ICCV*, 2019.
- [38] Mihir Prabhudesai, Tsung-Wei Ke, Alexander C Li, Deepak Pathak, and Katerina Fragkiadaki. Diffusion-tta: Test-time adaptation of discriminative models via generative feedback. *NeurIPS*, 2023.
- [39] Alec Radford, Jong Wook Kim, Chris Hallacy, Aditya Ramesh, Gabriel Goh, Sandhini Agarwal, Girish Sastry, Amanda Askell, Pamela Mishkin, Jack Clark, et al. Learning transferable visual models from natural language supervision. In *ICML*. PMLR, 2021.
- [40] Aditya Ramesh, Prafulla Dhariwal, Alex Nichol, Casey Chu, and Mark Chen. Hierarchical text-conditional image generation with clip latents. *arXiv preprint arXiv:2204.06125*, 2022.
- [41] Sylvestre-Alvise Rebuffi, Hakan Bilen, and Andrea Vedaldi. Learning multiple visual domains with residual adapters. *NeurIPS*, 2017.
- [42] Elad Richardson, Yuval Alaluf, Or Patashnik, Yotam Nitzan, Yaniv Azar, Stav Shapiro, and Daniel Cohen-Or. Encoding in style: a stylegan encoder for image-to-image translation. In *CVPR*, 2021.
- [43] Robin Rombach, Andreas Blattmann, Dominik Lorenz, Patrick Esser, and Björn Ommer. High-resolution image synthesis with latent diffusion models. In *CVPR*, 2022.
- [44] Christoph Schuhmann, Romain Beaumont, Richard Vencu, Cade Gordon, Ross Wightman, Mehdi Cherti, Theo Coombes, Aarush Katta, Clayton Mullis, Mitchell Wortsman, et al. Laion-5b: An open large-scale dataset for training next generation image-text models. *Advances in Neural Information Processing Systems*, 35:25278–25294, 2022.

- [45] Yujun Shen, Jinjin Gu, Xiaoou Tang, and Bolei Zhou. Interpreting the latent space of gans for semantic face editing. In *CVPR*, 2020.
- [46] Ken Shoemake. Animating rotation with quaternion curves. In *Proceedings of the 12th annual conference on Computer graphics and interactive techniques*, pages 245–254, 1985.
- [47] Jascha Sohl-Dickstein, Eric Weiss, Niru Maheswaranathan, and Surya Ganguli. Deep unsupervised learning using nonequilibrium thermodynamics. In *ICML*. PMLR, 2015.
- [48] Jiaming Song, Chenlin Meng, and Stefano Ermon. Denoising diffusion implicit models. *ICLR*, 2021.
- [49] Yang Song and Stefano Ermon. Generative modeling by estimating gradients of the data distribution. *NeurIPS*, 2019.
- [50] Yang Song, Jascha Sohl-Dickstein, Diederik P Kingma, Abhishek Kumar, Stefano Ermon, and Ben Poole. Score-based generative modeling through stochastic differential equations. In *ICLR*, 2020.
- [51] Yang Song, Prafulla Dhariwal, Mark Chen, and Ilya Sutskever. Consistency models. *ICML*, 2023.
- [52] Omer Tov, Yuval Alaluf, Yotam Nitzan, Or Patashnik, and Daniel Cohen-Or. Designing an encoder for stylegan image manipulation. *ACM Transactions on Graphics (TOG)*, 2021.
- [53] Jianzhong Wang. *Geometric structure of high-dimensional data and dimensionality reduction*. Springer, 2012.
- [54] Jindong Wang, Cuiling Lan, Chang Liu, Yidong Ouyang, Tao Qin, Wang Lu, Yiqiang Chen, Wenjun Zeng, and Philip Yu. Generalizing to unseen domains: A survey on domain generalization. *IEEE Transactions on Knowledge and Data Engineering*, 2022.
- [55] Tengfei Wang, Yong Zhang, Yanbo Fan, Jue Wang, and Qifeng Chen. High-fidelity gan inversion for image attribute editing. In *CVPR*, 2022.
- [56] Ting-Chun Wang, Ming-Yu Liu, Andrew Tao, Guilin Liu, Jan Kautz, and Bryan Catanzaro. Few-shot video-to-video synthesis. In *NeurIPS*, 2019.
- [57] Tianyi Wei, Dongdong Chen, Wenbo Zhou, Jing Liao, Weiming Zhang, Lu Yuan, Gang Hua, and Nenghai Yu. E2style: Improve the efficiency and effectiveness of stylegan inversion. *IEEE TIP*, 2022.
- [58] Kyle W Willett, Chris J Lintott, Steven P Bamford, Karen L Masters, Brooke D Simmons, Kevin RV Casteels, Edward M Edmondson, Lucy F Fortson, Sugata Kaviraj, William C Keel, et al. Galaxy zoo 2: detailed morphological classifications for 304 122 galaxies from the sloan digital sky survey. *Monthly Notices of the Royal Astronomical Society*, 435(4):2835–2860, 2013.
- [59] Junde Wu, Rao Fu, Huihui Fang, Yu Zhang, Yehui Yang, Haoyi Xiong, Huiying Liu, and Yanwu Xu. Medsegdiff: Medical image segmentation with diffusion probabilistic model. In *Medical Imaging with Deep Learning*, pages 1623–1639. PMLR, 2024.
- [60] KE Wu, KK Yang, R van den Berg, JY Zou, AX Lu, and AP Amini. Protein structure generation via folding diffusion; 2022. *arXiv preprint arXiv:2209.15611*.
- [61] Weihao Xia, Yulun Zhang, Yujiu Yang, Jing-Hao Xue, Bolei Zhou, and Ming-Hsuan Yang. Gan inversion: A survey. *IEEE TPAMI*, 2022.
- [62] Duo Xu, Stella SR Offner, Robert Gutermuth, Michael Y Grudić, Dávid Guszejnov, and Philip F Hopkins. Predicting the radiation field of molecular clouds using denoising diffusion probabilistic models. *The Astrophysical Journal*, 958(1):97, 2023.
- [63] Duo Xu, Jonathan C Tan, Chia-Jung Hsu, and Ye Zhu. Denoising diffusion probabilistic models to predict the density of molecular clouds. *The Astrophysical Journal*, 950(2):146, 2023.
- [64] Yongqi Yang, Ruoyu Wang, Zhihao Qian, Ye Zhu, and Yu Wu. Diffusion in diffusion: Cyclic one-way diffusion for text-vision-conditioned generation. *ICLR*, 2024.
- [65] Fisher Yu, Ari Seff, Yinda Zhang, Shuran Song, Thomas Funkhouser, and Jianxiong Xiao. Lsun: Construction of a large-scale image dataset using deep learning with humans in the loop. *arXiv preprint arXiv:1506.03365*, 2015.
- [66] Lily Zhang, Mark Goldstein, and Rajesh Ranganath. Understanding failures in out-of-distribution detection with deep generative models. In *ICML*. PMLR, 2021.

- [67] Min Zhao, Fan Bao, Chongxuan Li, and Jun Zhu. Egsde: Unpaired image-to-image translation via energy-guided stochastic differential equations. *NeurIPS22*, 2022.
- [68] Shanshan Zhao, Mingming Gong, Tongliang Liu, Huan Fu, and Dacheng Tao. Domain generalization via entropy regularization. *NeurIPS*, 2020.
- [69] Kaiyang Zhou, Yongxin Yang, Timothy Hospedales, and Tao Xiang. Learning to generate novel domains for domain generalization. In *ECCV*, 2020.
- [70] Kaiyang Zhou, Ziwei Liu, Yu Qiao, Tao Xiang, and Chen Change Loy. Domain generalization in vision: A survey. *arXiv preprint arXiv:2103.02503*, 2021.
- [71] Shuheng Zhou, Philipp Rütimann, Min Xu, and Peter Bühlmann. High-dimensional covariance estimation based on gaussian graphical models. *The Journal of Machine Learning Research*, 2011.
- [72] Jiapeng Zhu, Yujun Shen, Deli Zhao, and Bolei Zhou. In-domain gan inversion for real image editing. In *ECCV*. Springer, 2020.
- [73] Jun-Yan Zhu, Philipp Krähenbühl, Eli Shechtman, and Alexei A Efros. Generative visual manipulation on the natural image manifold. In *ECCV*. Springer, 2016.
- [74] Ye Zhu, Yu Wu, Zhiwei Deng, Olga Russakovsky, and Yan Yan. Boundary guided learning-free semantic control with diffusion models. In *NeurIPS*, 2023.
- [75] Ye Zhu, Yu Wu, Kyle Olszewski, Jian Ren, Sergey Tulyakov, and Yan Yan. Discrete contrastive diffusion for cross-modal music and image generation. In *ICLR*, 2023.

## A Appendix / supplemental material

We structure the appendices as follows: We provide a detailed discussion on the related work in Appendix B. In Appendix C, we present the background of deterministic diffusion models. In Appendix D, we provide detailed proof for the lemmas used in Sec. 2 of the main paper as part of analytical studies. Meanwhile, Appendix D includes the necessary background on the geometric properties of high-dimensional Gaussians. More latent sampling methods are discussed in Appendix E. Appendix F includes additional details about the generative experiments on unseen OOD domains.

## B Related Work

Due to the space limitations in the main paper, we present a detailed discussion of related work in our appendices.

### B.1 Generalization in Generative Models

Domain Generalization [54] that aims to generalize models' ability to extended data distributions has been an important research topic in broad machine learning area [13, 68, 70, 35, 33], with various computer vision applications such as recognition [37, 41], detection [66] and segmentation [22, 14]. In the vision generative field, it becomes an even more challenging task with the extra demand to sample from the generalized distributions. One popular recent trend in the computer vision community is scaling up the model and dataset sizes as the most intuitive and obvious solutions [40, 20, 43]. Another scenario to study the domain generalization of generative models is within the few-shot scenario, where we only have a limited amount of data compared to the training set. In this case, fine-tuning the given model on the limited images [29] is the most straightforward way to go.

Our work falls into the second category: provided with a pre-trained model and a small set of unseen images different from the model's training domain, we seek to better understand the generalization abilities of DDPMs.

### B.2 Diffusion Models and Deterministic Variants

Diffusion Models (DMs) [47, 19, 49] are the state-of-the-art generative models for data synthesis in images [40, 43, 36, 16, 11, 23], videos [21], and audio [30, 75, 34]. There are currently two mainstream fundamental formulations of diffusion models, i.e., the denoising diffusion probabilistic models (DDPMs) [19] and score-based models [50]. One common perspective to understand both formulations is to consider the data generation as solving stochastic differential equations (SDEs), which characterize a stochastic process. Based on vanilla models, both branch develops their own deterministic variants, i.e., denoising diffusion implicit models (DDIMs) [48] and consistency models [51], with their core idea to follow the marginal distributions in denoising. Compared to initial DDPMs and Score-based DMs with ancestral sampling, the deterministic variants are solving ODEs instead of SDEs and largely accelerate the generation speed with fewer steps.

We leverage the deterministic variant (DDIMs [48]) as the tool to achieve bidirectional transition between latent noisy space and data space in this work.

### B.3 Latent Space of Deep Generative Models

Comprehensive studies of latent space of generative models [26, 1, 12] help to better understand the model and also benefit downstream tasks such as data editing and manipulation [73, 45, 31, 72]. A large portion of work has been exploring this problem within the context of GAN inversion [61], where the typical methods can be mainly divided into either learning-based [73, 42, 57, 3] or optimization-based categories [1, 2, 24, 10]. More recently, with the growing popularity of diffusion models, researchers have also focused on the latent space understanding of DMs for better synthesis qualities or semantic control [43, 74, 64].

Our work also contributes to a better understanding of latent spaces, and aims to introduce a new synthesis paradigm to explore the intrinsic potential of DMs.



## B.4 Diffusion Models in Science

While DMs have been extensively applied in data generation and editing within the multimodal context [43, 21, 75, 64, 74], recent works have extended their application domains to scientific explorations, such as astrophysics [63, 62], medical imaging [28, 59], and biology [60]. Compared to conventional computer vision applications, scientific tasks usually exhibit several distinct features. For instance, data acquisition and annotation are generally more expensive due to their scientific nature, resulting in a relatively smaller amount of available data for experiments. Additionally, the evaluation of these works adheres to established conventions within their respective contexts, which are usually different from image synthesis evaluation based on perceptual quality.

Our work also experiments with several astrophysical datasets to showcase the potential of applying our proposed paradigm and method to such specific domains with limited data.

## C Deterministic Diffusion

Our analytical studies and methodology designs are built upon a specific variant of diffusion formulations, i.e., the deterministic diffusion process. While the original DDPMs involve a stochastic process for data generation via denoising (*i.e.*, the same latent encoding will output different denoised images every time after the same generative chain), there is a variant of diffusion model that allows us to perform the denoising process in a deterministic way, known as the Denoising Diffusion Implicit Models (DDIMs) [48]. DDIMs were initially proposed for the purpose of speeding up the denoising process, however, later research works extend DDIMs from faster sampling application to other usages including the inversion technique to convert a raw image to its arbitrary latent space in a deterministic and tractable way. As briefly stated in our main paper, the core theoretical difference between DDIMs and DDPMs lies within the nature of forward process, which modifies a Markovian process to a non-Markovian one.

The key idea in the context of non-Markovian forward is to consider a family of  $\mathcal{Q}$  of inference distributions, indexed by a real vector  $\sigma \in \mathbb{R}_{\geq 0}^T$ :

$$q_{\sigma}(\mathbf{x}_{1:T}|\mathbf{x}_0) := q_{\sigma}(\mathbf{x}_T|\mathbf{x}_0) \prod_{t=2}^T q_{\sigma}(\mathbf{x}_{t-1}|\mathbf{x}_t, \mathbf{x}_0), \quad (5)$$

where  $q_{\sigma}(\mathbf{x}_T|\mathbf{x}_0) = \mathcal{N}(\sqrt{\alpha_T}\mathbf{x}_0, (1 - \alpha_T)\mathbf{I})$  and for all  $t > 1$ ,

$$q_{\sigma}(\mathbf{x}_{t-1}|\mathbf{x}_t, \mathbf{x}_0) = \mathcal{N}(\sqrt{\alpha_{t-1}}\mathbf{x}_0 + \sqrt{1 - \alpha_{t-1} - \sigma_t^2} \cdot \frac{\mathbf{x}_t - \sqrt{\alpha_t}\mathbf{x}_0}{\sqrt{1 - \alpha_t}}, \sigma_t^2\mathbf{I}). \quad (6)$$

The choice of mean function from Eqn. 6 ensures that  $q_{\sigma}(\mathbf{x}_t|\mathbf{x}_0) = \mathcal{N}(\sqrt{\alpha_t}\mathbf{x}_0, (1 - \alpha_t)\mathbf{I})$  for all  $t$ , so that it defines a joint inference distribution that matches the ‘‘marginals’’ as desired. The non-Markovian forward process can be derived from Bayes’ rule:

$$q_{\sigma}(\mathbf{x}_t|\mathbf{x}_{t-1}, \mathbf{x}_0) = \frac{q_{\sigma}(\mathbf{x}_{t-1}|\mathbf{x}_t, \mathbf{x}_0)q_{\sigma}(\mathbf{x}_t|\mathbf{x}_0)}{q_{\sigma}(\mathbf{x}_{t-1}|\mathbf{x}_0)}. \quad (7)$$

In fact, in the original paper, the authors also explicitly stated that: ‘‘The forward process from Eqn. 7 is also Gaussian (although we do not use this fact for the remainder of this paper)’’.<sup>6</sup> While this Gaussian property was not emphasized and leveraged in the DDIMs paper, we find it useful in our context to explore the representation and generalization ability of pre-trained DDPMs.

In particular, the hyper-parameters for Gaussian scheduling  $\alpha$  and  $\beta$  in the context of DDIMs are slightly different from the original formulation in DDPMs [19]. Denote the original sequences from DDPMs as  $\alpha'_t$ , then the  $\alpha_t$  in this work follows the definition of DDIMs to be  $\alpha_t = \prod_{t=1}^T \alpha'_t$ .

In addition to DDIMs, we note that the score-based formulation has also recently marked a deterministic variant, namely the Consistency Models [51]. The core idea of the consistency model is, to some extent, similar to DDIMs, which allows the vanilla score-based stochastic diffusion models to achieve ‘‘one-step’’ denoising, by following the marginal distributions.

As mentioned in our main paper, the deterministic diffusion is mainly used as a tool in this work for our proposed tuning-free paradigm.

<sup>6</sup>This paper refer to the DDIM paper [48].

Table 3: **Reconstruction results for arbitrary images via deterministic diffusion.** We use an iDDPM [36] trained on AFHQ-Dog and 1K testing OOD images to compute the MAE (mean absolute error) reconstruction metric. Note DDIMs [48] was initially proposed to accelerate DDPMs sampling, but have not been studied in this OOD reconstruction setting.

Method	Recons. Domain	MAE ( $\downarrow$ )
pSp [42]	CelebA (ID)	0.079
e4e [52]	CelebA (ID)	0.092
ReStyle [3]	CelebA (ID)	0.089
HFGI [55]	CelebA (ID)	0.062
DDIMs [48]	Dog (ID)	$0.073 \pm 6e-4$
	CelebA (OOD)	$0.073 \pm 8e-4$
	Church (OOD)	$0.074 \pm 8e-4$
	Bedroom (OOD)	$0.072 \pm 7e-4$
	Galaxy (OOD)	$0.067 \pm 1e-3$
	Radiation (OOD)	$0.077 \pm 9e-4$

## D Detailed Proofs and Geometric Properties

In this section, we provide detailed proof for the lemmas in Sec. 2. Particularly, Lemma 2.2 is a known property in high-dimensional Gaussian studies.

### D.1 Proof of Lemma 2.1

We restate the lemma below, and provide the detailed proof, which has been introduced in the original DDIM paper [48].

**Lemma D.1.** For  $q_\sigma(\mathbf{x}_{1:T}|\mathbf{x}_0)$  defined in Eqn. 1 and  $q_\sigma(\mathbf{x}_{t-1}|\mathbf{x}_t, \mathbf{x}_0)$  defined in Eqn. 2, we have:

$$q_\sigma(\mathbf{x}_t|\mathbf{x}_0) = \mathcal{N}(\sqrt{\alpha_t}\mathbf{x}_0, (1 - \alpha_t)\mathbf{I}). \quad (8)$$

*Proof:*

Assume for any  $t \leq T$ ,  $q_\sigma(\mathbf{x}_t|\mathbf{x}_0) = \mathcal{N}(\sqrt{\alpha_t}\mathbf{x}_0, (1 - \alpha_t)\mathbf{I})$  holds, if:

$$q_\sigma(\mathbf{x}_{t-1}|\mathbf{x}_0) = \mathcal{N}(\sqrt{\alpha_{t-1}}\mathbf{x}_0, (1 - \alpha_{t-1})\mathbf{I}), \quad (9)$$

then we can prove that the statement with an induction argument for  $t$  from  $T$  to 1, since the base case ( $t = T$ ) already holds.

First, we have that

$$q_\sigma(\mathbf{x}_{t-1}|\mathbf{x}_0) := \int_{\mathbf{x}_t} q_\sigma(\mathbf{x}_t|\mathbf{x}_0)q_\sigma(\mathbf{x}_{t-1}|\mathbf{x}_t, \mathbf{x}_0)d\mathbf{x}_t, \quad (10)$$

$$q_\sigma(\mathbf{x}_t|\mathbf{x}_0) = \mathcal{N}(\sqrt{\alpha_t}\mathbf{x}_0, (1 - \alpha_t)\mathbf{I}), \quad (11)$$

$$q_\sigma(\mathbf{x}_{t-1}|\mathbf{x}_t, \mathbf{x}_0) = \mathcal{N}(\sqrt{\alpha_{t-1}}\mathbf{x}_0 + \sqrt{1 - \alpha_{t-1} - \sigma_t^2} \cdot \frac{\mathbf{x}_t - \sqrt{\alpha_t}\mathbf{x}_0}{\sqrt{1 - \alpha_t}}, \sigma_t^2\mathbf{I}). \quad (12)$$

According to [6] 2.3.3 *Bayes' theorem for Gaussian variables*, we know that  $q_\sigma(\mathbf{x}_{t-1}|\mathbf{x}_0)$  is also Gaussian, denoted as  $\mathcal{N}(\mu_{t-1}, \Sigma_{t-1})$  where:

$$\mu_{t-1} = \sqrt{\alpha_{t-1}}\mathbf{x}_0 + \sqrt{1 - \alpha_{t-1} - \sigma_t^2} \cdot \frac{\sqrt{\alpha_t}\mathbf{x}_0 - \sqrt{\alpha_t}\mathbf{x}_0}{\sqrt{1 - \alpha_t}} = \sqrt{\alpha_{t-1}}\mathbf{x}_0, \quad (13)$$

$$\Sigma_{t-1} = \sigma_t^2\mathbf{I} + \frac{1 - \alpha_{t-1} - \sigma_t^2}{1 - \alpha_t}(1 - \alpha_t)\mathbf{I} = (1 - \alpha_{t-1})\mathbf{I}. \quad (14)$$

Therefore,  $q_\sigma(\mathbf{x}_{t-1}|\mathbf{x}_0) = \mathcal{N}(\sqrt{\alpha_{t-1}}\mathbf{x}_0, (1 - \alpha_{t-1})\mathbf{I})$ , which allows to apply the induction argument.

*Q.E.D*

## D.2 Proof of Lemma 4.2

**Lemma D.2.** *Mixtures of spherical Gaussians in  $d$  dimensions can be separated provided their centers are separated by more than  $d^{\frac{1}{4}}$  distance (i.e, a separation of  $\Omega(d^{\frac{1}{4}})$ ), and even by  $\Omega(1)$  separation with more sophisticated algorithms.*

*Proof:*

According to existing established understanding (Lemma 2.8 from [7]), for a  $d$ -dimensional spherical Gaussian of variance 1, all but  $\frac{4}{c^2}e^{-\frac{c^2}{4}}$  fraction of its mass is within the annulus  $\sqrt{d-1} - c \leq r \leq \sqrt{d-1} + c$  for any  $c > 0$ , as illustrated in Fig. 5.

Given two spherical unit variance Gaussians, we have most of the probability mass of each Gaussian lies on an annulus of width  $O(1)$  at radius  $\sqrt{d-1}$ . Also,  $e^{-|x|^2/2}$  factors into  $\prod_i e^{-x_i^2/2}$  and almost all of the mass is within the slab  $\{x | -c \leq x_1 \leq c\}$ , for  $c \in O(1)$ .

Now consider picking arbitrary samples and their separability. After picking the first sample  $\mathbf{x}$ , we can rotate the coordination system to make the first axis point towards  $\mathbf{x}$ . Next, independently pick a second point  $\mathbf{y}$  also from the first Gaussian. The fact that almost all of the mass of the Gaussian is within the slab  $\{x | -c \leq x_1 \leq c, c \in O(1)\}$  at the equator says that  $\mathbf{y}$ 's component along  $\mathbf{x}$ 's direction is  $O(1)$  with high probability, which indicates  $\mathbf{y}$  should be nearly perpendicular to  $\mathbf{x}$ , and thus we have  $|\mathbf{x} - \mathbf{y}| \approx \sqrt{|\mathbf{x}|^2 + |\mathbf{y}|^2}$ .

More precisely, we note  $\mathbf{x}$  is at the North Pole after the coordination rotation with  $\mathbf{x} = (\sqrt{d} \pm O(1), 0, \dots)$ . At the same time,  $\mathbf{y}$  is almost on the equator, we can further rotate the coordinate system so that the component of  $\mathbf{y}$  that is perpendicular to the axis of the North Pole is in the second coordinate, with  $\mathbf{y} = (O(1), \sqrt{d} \pm O(1), \dots)$ . Thus we have:

$$(\mathbf{x} - \mathbf{y})^2 = d \pm O(\sqrt{d}) + d \pm O(\sqrt{d}) = 2d \pm O(\sqrt{d}), \quad (15)$$

and  $|\mathbf{x} - \mathbf{y}| = \sqrt{(2d) \pm O(1)}$ .

Given two spherical unit variance Gaussians with centers  $\mathbf{p}$  and  $\mathbf{q}$  separated by a distance  $\delta$ , the distance between a randomly chosen point  $\mathbf{x}$  from the first Gaussian and a randomly chosen point  $\mathbf{y}$  from the second is close to  $\sqrt{\delta^2 + 2d}$ , since  $\mathbf{x} - \mathbf{p}$ ,  $\mathbf{p} - \mathbf{q}$ , and  $\mathbf{q} - \mathbf{y}$  are nearly mutually perpendicular, with:

$$|\mathbf{x} - \mathbf{y}|^2 \approx \delta^2 + |\mathbf{z} - \mathbf{q}|^2 + |\mathbf{q} - \mathbf{y}|^2 = \delta^2 + 2d \pm O(\sqrt{d}). \quad (16)$$

To ensure that the distance between two points picked from the same Gaussian are closer to each other than two points picked from different Gaussians requires that the upper limit of the distance between a pair of points from the same Gaussian is at most the lower limit of distance between points from different Gaussians. This requires the following criterion to be satisfied:

$$\sqrt{2d} + O(1) \leq \sqrt{2d + \delta^2} - O(1), \quad (17)$$

which holds when  $\delta \in \Omega(d^{1/4})$ .

Thus, mixtures of spherical Gaussians can be separated provided their centers are separated by more than  $d^{1/4}$ .

*Q.E.D*

## D.3 Geometric Properties

We consistently observe three geometric properties for the inverted OOD latent encodings. We provide a more detailed discussion on what each property implies in this sub-section.

Recall the three geometric properties as below:

**Observation 1:** *For any OOD sample pairs  $\mathbf{x}_{inv,i}^{out}$  and  $\mathbf{x}_{inv,j}^{out}$  from the sample set, the Euclidean distance between these two points is approximately a constant  $d_o$ .*

**Observation 2:** *For any three OOD samples  $\mathbf{x}_{inv,i}^{out}$ ,  $\mathbf{x}_{inv,j}^{out}$  and  $\mathbf{x}_{inv,k}^{out}$  from the sample set, the angle formed between  $\mathbf{x}_{inv,k}^{out} \rightarrow \mathbf{x}_{inv,i}^{out}$  and  $\mathbf{x}_{inv,k}^{out} \rightarrow \mathbf{x}_{inv,j}^{out}$  is always around  $60^\circ$ .*

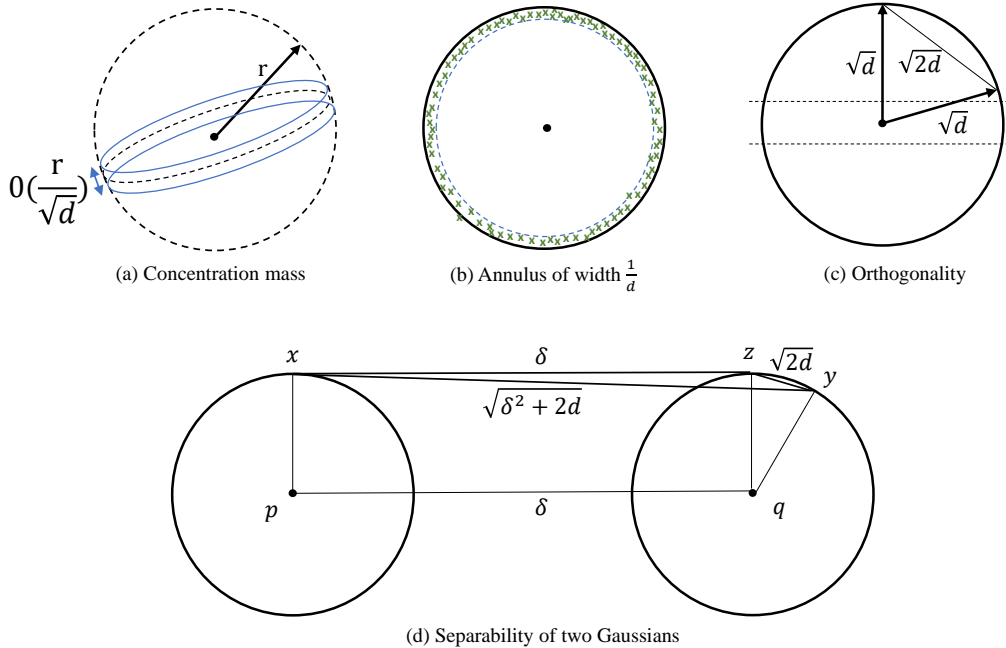


Figure 5: **Illustration of various geometric properties of high-dimensional Gaussians.** (a) and (b) show the probability concentration mass is mainly centered around a thin annulus around the equator. (c) illustrates the geometric observation on the orthogonality of sample pairs. (d) illustrates the idea of separating two Gaussian distributions in high-dimensional spaces.

**Observation 3:** For any OOD sample pairs  $\mathbf{x}_{inv,i}^{out}$  and  $\mathbf{x}_{inv,j}^{out}$  from the sample set, let  $O$  denote the origin in the high-dimensional space, the angle formed between  $O\mathbf{x}_{inv,i}^{out}$  and  $O\mathbf{x}_{inv,j}^{out}$  is always around  $90^\circ$ .

For the first observation, when the sample pairs keep approximately the same distance, the direct implication is that those samples are likely to be drawn from some convex region in the high-dimensional space [53]. One typical example is the spherical structure, where every data points exhibit an equal distance from the center.

The second geometric property suggests that the unknown samples could lie on a regular lattice near a low-dimensional manifold or sub-manifold, where the local geometry of the manifold is approximately Euclidean. However, a less evident implication is that for samples drawn from a high-dimensional Gaussian, this property also holds, as detailed in the next section D.4, and illustrated in Fig. 5(c).

The third geometry property implies that the sample points might be isotropic in nature, who are rotationally symmetric around any point in the space. Therefore, any two points drawn from the distribution are equally likely to lie along any direction in the space. This property is also observed for a high-dimensional Gaussian [7], whose covariance matrix is proportional to the identity matrix.

We acknowledge that to deduce a distribution in high-dimensional space solely based on its geometric properties is very challenging, and there may exist other complex distributions that exhibit similar properties we have observed. However, combined with our theoretical analysis and empirical observations, the OOD Gaussian assumption seems to hold well. Explicitly, we find the above geometric properties do not hold for images  $\mathbf{x}_0$  from the data space. For instance, the angle of samples to the origin is approximately  $75^\circ$  rather than  $90^\circ$ .

## D.4 High-Dimensional Gaussian

Gaussian in high-dimensional space establishes various characteristic behaviors that are not obvious and evident in low-dimensionality. A better understanding of those unique geometric and probabilistic behaviors is critical to investigate the latent spaces of DDMs, since all the intermediate latent spaces along the denoising chain are Gaussian as demonstrated and proved in our previous sections.

We present below several properties of high-dimensional Gaussian from [7], note those are known and established properties, we therefore omit the detailed proofs in this supplement, and ask readers to refer to the original book if interested.

**Property D.1.** *The volume of a high-dimensional sphere is essentially all contained in a thin slice at the equator and is simultaneously contained in a narrow annulus at the surface, with essentially no interior volume. Similarly, the surface area is essentially all at the equator.*

This property above is illustrated in Fig. 5(a)(b), where the sampled ID encodings are presented in a narrow annulus.

**Lemma D.2.** *For any  $c > 0$ , the fraction of the volume of the hemisphere above the plane  $x_1 = \frac{c}{\sqrt{d-1}}$  is less than  $\frac{2}{c}e^{-\frac{c^2}{2}}$ .*

**Lemma D.3.** *For a  $d$ -dimensional spherical Gaussian of variance 1, all but  $\frac{4}{c^2}e^{-c^2/4}$  fraction of its mass is within the annulus  $\sqrt{d-1} - c \leq r \leq \sqrt{d-1} + c$  for any  $c > 0$ .*

The lemmas above imply that the volume range of the concentration mass above the equator is in the order of  $O(\frac{r}{\sqrt{d}})$ , also within an annulus of constant width and radius  $\sqrt{d-1}$ . In fact, the probability mass of the Gaussian as a function of  $r$  is  $g(r) = r^{d-1}e^{-r^2/2}$ . Intuitively, this states the fact that the samples from a high-dimensional Gaussian distribution are mainly located within a manifold, which matches our second geometric observation.

**Lemma D.4.** *The maximum likelihood spherical Gaussian for a set of samples is the one over center equal to the sample mean and standard deviation equal to the standard deviation of the sample.*

The above lemma is used as the theoretical justification for the proposed empirical search method in [74]. We also adopt the search method using the Gaussian radius for identifying the operational latent space along the denoising chain to perform the OOD sampling.

**Property D.5.** *Two randomly chosen points in high dimension are almost surely nearly orthogonal.*

The above property corresponds to the *Observation 3*, where two inverted OOD samples consistently form a  $90^\circ$  angle at the origin.

## E More Details about the Latent Sampling Methods

We present here the detailed algorithms for our proposed latent sampling methods, and discuss many other sampling methods that we have tested during experiments.

### E.1 Algorithms

While we have described the procedure of our proposed latent sampling method in Sec. 3, the following Algo. 1 and Algo. 2 include details of the overall pipeline and the geometric optimizations, respectively.

### E.2 Other Sampling Methods

In addition to the main sampling method introduced in the main paper, we have tested many other sampling methods for mining the qualified OOD latent encodings.

We list those sampling methods below as extra information and provide a brief discussion for each.

**Approach 1: Estimated Gaussian Sampling.** An intuitive way to achieve the OOD sampling based on our analytical understanding from Sec. 2 is to directly fit the latent encodings with a Gaussian distribution and then sample from the estimated Gaussian. However, we note that the

---

**Algorithm 1** Domain Discovery and Expansion within DDPMs

---

**Input:**  $N$  raw images  $\mathbf{x}_{od}$  from the target unseen domain  $\mathcal{D}_{od}$ , a pre-trained DDPM  $p$  for domain  $\mathcal{D}_{id}$ , target latent step  $t$  for sampling ( $t$  is a pre-set hyper-parameter discussed in Sec. 4.2).  
**Output:** images of the unseen target  $\mathbf{x}'_{od} \in \mathcal{D}_{od}$   
*// Step 1: get the inverted OOD encodings  $\mathbf{x}_{od,t}$*   
Define  $\{\tau_s\}_{s=1}^{S_{inv}}$  s.t.  $\tau_1 = 0, \tau_{S_{inv}} = t$   
**for**  $i = 1, 2, \dots, N$  **do**  
  **for**  $s = 1, 2, \dots, S_{inv} - 1$  **do**  
     $\epsilon \leftarrow p(\mathbf{x}_{od,\tau_s}^i, \tau_s)$   
     $\mathbf{x}_{od,\tau_{s+1}}^i = \sqrt{\alpha_{\tau_s}} \mathbf{x}_{od,\tau_s}^i + \sqrt{1 - \alpha_{\tau_s}} \epsilon$   
  **end for**  
  Save the OOD latent  $\mathbf{x}_{od,\tau_{S_{inv}}}^i$  as  $\{\mathbf{x}_{od,t}\}_{i=1,\dots,N}$   
**end for**  
*// Step 2: get new OOD encodings  $\mathbf{x}'_{od,t}$*   
 $\mu_{est} \leftarrow \text{Mean}(\{\mathbf{x}_{od,t}^1, \mathbf{x}_{od,t}^2, \dots, \mathbf{x}_{od,t}^N\})$   
 $\sigma_{est}^2 \leftarrow \text{Var}(\{\mathbf{x}_{od,t}^1, \mathbf{x}_{od,t}^2, \dots, \mathbf{x}_{od,t}^N\})$   
**while true do**  
   $\bar{\mathbf{x}}_{od,t} \sim \mathcal{N}(\mu_{est}, \sigma_{est}^2)$   
   $\mathbf{x}_{od,t} \sim \{\mathbf{x}_{od,t}\}_{i=1,\dots,N}$   
   $\mathbf{x}'_{od,t} \leftarrow \text{Slerp}(\mathbf{x}_{od,t}, \bar{\mathbf{x}}_{od,t})$   
  *// geometric optimization*  
  **if** Pass the geometric optimization in Algo. 2 **then**  
    **break**  
  **end if**  
**end while**  
*// Step 3: get denoised  $\mathbf{x}'_{od} \in \mathcal{D}_{od}$*   
 $\mathbf{x}'_{od} \leftarrow p(\mathbf{x}'_{od,t}, t)$ 

---

high-dimensional Gaussian estimation itself remains as a challenging and complex research topic, especially in a multi-variant case [71, 4]. In general, a reliable estimation of means and variances requires data samples at least 10 times the dimensionality, known as the “rule of ten” [25], which contradicts our few-shot setup. Empirically, we also observe that the synthesis quality with vanilla Gaussian sampling is not very promising. The key reason for this is the gap between the theoretical foundation and practical model training, as also discussed in our main paper.

**Approach 2: MCMC Sampling.** As an improved statistical method over vanilla Gaussian sampling, we also tested the MCMC sampling technique, which should provide a better and more precise estimation of the distribution based on the inverted latent samples. However, one practical challenge we encountered during the experiments is that MCMC sampling takes an extremely long time for high-dimensional data in this context (i.e., several days using Metropolis-Hastings and Gibbs, which even exceeds the time required to tune the entire model). Therefore, we do not recommend or include this method in our main paper.

**Approach 3: Gaussian Sampling w/ Geometric Optimization.** A more practical implementation of the Gaussian sampling is to leverage the geometric properties as the domain-specific criteria to further optimize the quality of latent encodings, just as described in Algo. 2. We note this improves over the vanilla Gaussian sampling, but still qualitatively suffers from the mode interference issue.

## F More Details for Generative Experiments

### F.1 Background and Evaluation about the Astrophysical Data

**Galaxy Data.** The images from the GalaxyZoo dataset [58] are observation data of galaxies that belong to one of six categories - elliptical, clockwise spiral, anticlockwise spiral, edge-on, star/don’t know, or merger. The original data format of those galaxy images are also RGB images, thus



---

**Algorithm 2** Latent Sampling with Geometric Optimizations

---

**Input:** A sampled OOD latent encoding  $x'_{od,t}$ ,  $N$  inverted OOD latent  $\{x_{od,t}^1, x_{od,t}^2, \dots, x_{od,t}^N\}$ , distance tolerance  $\omega_d$ , angle tolerance  $\omega_a$ ,  $N_{ref}$  OOD reference samples

**Output:** True or False

*// Step 1: get pair-wise distance from the inverted OOD encodings  $x_{od,t}$*

$d_{od} \leftarrow 0$

**for**  $i = 1, 2, \dots, n$  **do**

$(p, q) \leftarrow \text{RandomInt}(0, N - 1)$

$d_{od} += \text{Euclidiien\_distance}(x_{od,t}^p, x_{od,t}^q)$

**end for**

$d_{od} \leftarrow d_{od}/n$

*// Step 2: Geometric optimization based on pre-defined tolerances*

**for**  $i = 1, \dots, N_{ref}$  **do**

$d \leftarrow \text{Euclidiien\_distance}(x_{od,t}^i, x'_{od,t})$

**if**  $d < d_{od} - \omega_d$  **or**  $d > d_{od} + \omega_d$  **then**

**return** *False*

**end if**

**end for**

**for**  $i = 1, \dots, N_{ref}$  **do**

$(p, q) \leftarrow \text{RandomInt}(0, N_{ref} - 1)$

$\varphi \leftarrow \text{Angle}(x'_{od,t} \vec{x}_{od,t}^p, x'_{od,t} \vec{x}_{od,t}^q)$

**if**  $\varphi < 60 - \omega_a$  **or**  $\varphi > 60 + \omega_a$  **then**

**return** *False*

**end if**

**end for**

**return** *True*

---

“somewhat” similar to natural images, but they contain important morphological information to study the galaxies in astronomy.

The evaluation of the synthesized galaxy data is based on the expertise of astrophysicists if they could reliably classify the generated images into one of the known categories.

**Radiation Data.** For the radiation data from [62], the original format is physical quantity instead of RGB images, which correspond to the dust emission.

Dust is a significant component of the interstellar medium in our galaxy, composed of elements such as oxygen, carbon, iron, silicon, and magnesium. Most interstellar dust particles range in size from a few molecules to 0.1 mm (100  $\mu\text{m}$ ), similar to micrometeoroids. The interaction of dust particles with electromagnetic radiation depends on factors like their cross-section, the wavelength of the radiation, and the nature of the grain, including its refractive index and size. The radiation process for an individual grain is defined by its emissivity, which is influenced by the grain’s efficiency factor and includes processes such as extinction, scattering, absorption, and polarization.

In RGB images of dust emission, different colors represent emissions at three wavelengths: blue for 4.5  $\mu\text{m}$ , green for 24  $\mu\text{m}$ , and red for 250  $\mu\text{m}$ . The blue color typically indicates short-wavelength dust emission from point sources, such as young stars or young stellar objects. The green color represents mid-wavelength dust emission from warm and hot dust. The red color signifies long-wavelength dust emission from cold dust.

Warm/hot dust emission (green) is usually found around stars, which appear as blue-colored dots. Since warm dust often mixes with cold dust on the outer edges of bubble structures, the resulting color is often yellowish. Cold dust extends farther from the stars, giving the background or areas outside star clusters a red appearance. In the case of massive star clusters, stellar feedback, such as radiation and stellar winds, can blow away the surrounding gas and dust, creating black or blank areas. Typically, RGB images show more extensive red emission with some orange/yellow emission, displaying filamentary and bubble structures, along with blue and/or white dotted point source emissions.

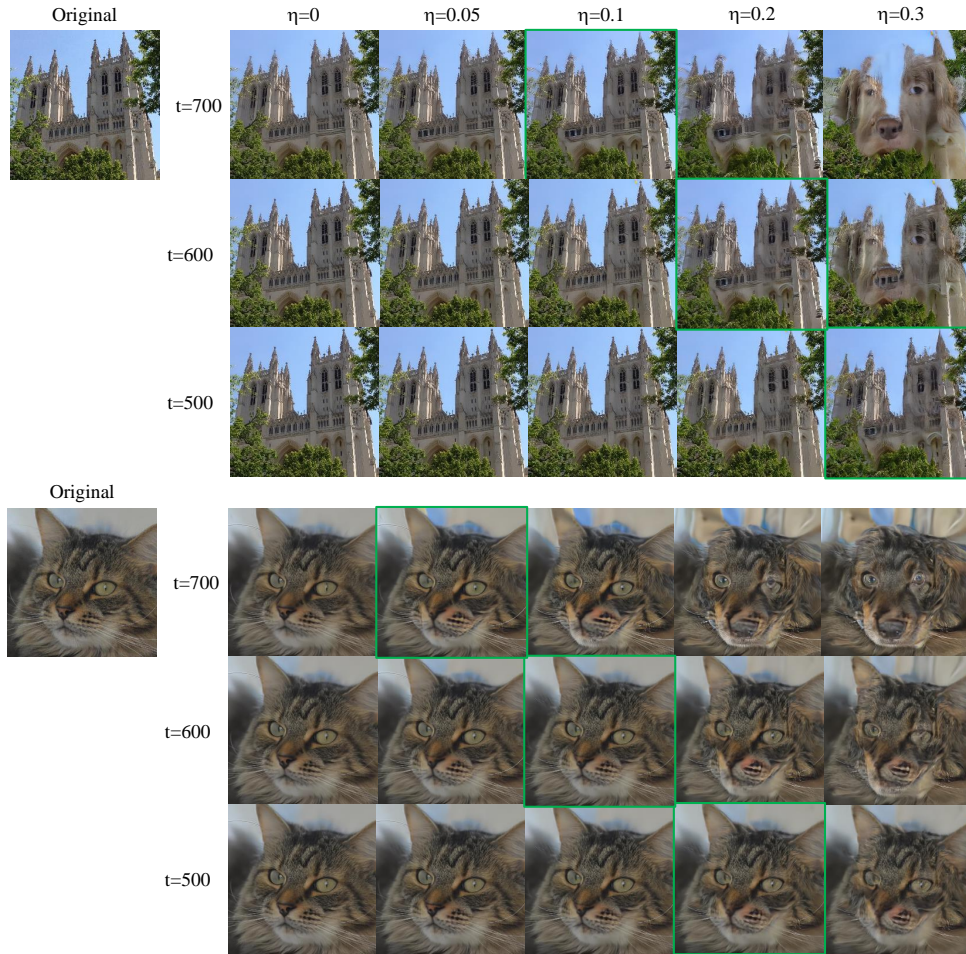


Figure 6: **Illustration of unseen trajectory bandwidth at different diffusion steps.** We show qualitative examples using the iDDPM [36] trained on AFHQ-Dog-256 as the base model, the examples of church and cat are both unseen domain images. The image in green boxes indicates the bandwidth we have empirically selected to preserve the reconstruction quality. Compared to the trained image domain (*i.e.*, *dogs*), *cats* have a smaller domain gap than *churches*. Different from the conventional understanding that a smaller domain gap is beneficial for better and easier generalization from a trained model, we observe a larger domain gap signifies a larger bandwidth, making it easier to perform the OOD sampling and synthesis.

The above background is considered as part of the underlying evaluation criteria when performing subjective evaluation on the quality of generated radiation data.

## F.2 More Experimental Results

We provide extended discussions in this section for the readers who are interested in more subtle experimental details.

### F.2.1 Discussion on the Latent Step $t$ , Stochasticity and Mode Interference

In our main paper, we briefly discuss the impact of the latent diffusion step  $t$  where we perform the inversion and OOD latent sampling. While we empirically find that  $t \approx 800$  is a reasonable range for the choice of  $t$ , we note there exists an entangled mechanism for the trade-off between the sampling difficulty and the mode interference issue.

For the diffusion step  $t$ , recent studies [74, 64] suggest that  $t$  characterizes the formation of image information at different stages of the denoising process. Intuitively, the early stage of the denoising process (e.g.,  $t > 800$ ) represents a rather chaotic process, the mixing step  $t_m$  [74] signifies a critical stage where the image semantic information starts to form, and the later stage where  $t$  is close to 0 demonstrates a stage during which more fine-grained pixel-level information are introduced to the final generated data. From the distribution point of view, the influence of  $t$  can be interpreted as the convergence of distributions, where  $t = T$  is a standard Gaussian by definition, thus the ID and OOD modes are more difficult to separate. However, as the denoising process gets closer to the real image space at  $t = 0$ , the sampling difficulty increases as the implicit distribution moves away from the standard Gaussian.

Meanwhile, the diffusion step  $t$  is not the only factor that impacts the trade-off between sampling difficulty and mode interference. While scarcely discussed in the main paper, we note the stochasticity of the denoising trajectory also plays a similar role as the diffusion step in this work. The stochasticity of the denoising trajectory in DMs has been proven to be generally beneficial in improving the synthesis quality [27, 29, 31, 74]. In this work, while we choose the  $\eta = 0$  for the main paper, a tolerance for a certain range of stochasticity allows us to follow a “relatively deterministic” denoising process  $p_{\eta=k}$ , with  $k \neq 0$ , instead of the completely deterministic  $p_i$ . We hereby refer to it as “bandwidth of the unseen trajectories,” denoted as  $\mathcal{B}_{\eta,t}$ , which can be used to quantify the “mode interference”. Another interpretation is to analog the trajectory bandwidth  $\mathcal{B}_{\eta,t}$  to the actual subspace volume occupied by the OOD latent samples. Fig. 6 shows more qualitative results for the bandwidth search in the reconstruction task and reveals its connection to the diffusion step  $t$ . Overall, the bandwidth is a hyper-parameter that relates to the base model and the unseen domains, and the diffusion step  $t$ , while the bandwidth gets larger at the latent spaces closer to the raw image domains, sampling from OOD unseen distributions also gets more difficult.

## F.2.2 Discussion on Model Designs

Among four base DDPMs we have tested, there are two architecture variants namely the improved DDPM [36] and vanilla DDPM [19]. The difference between the two variants lies within the scheduler design for the Gaussian perturbation kernels: improved DDPM uses a cosine scheduler while vanilla DDPM adopts a linear one. Our experiments suggest that iDDPM in general synthesizes images with better quality in terms of FID scores, which aligns with previous studies [36, 74]. One implication from the above observation is that the domain generalization abilities studied in this context is inherited from the performance of model’s original performance.

## F.2.3 More Qualitative Results

We show more qualitative samples from the CLIP-tuned methods in Fig. 7 and Fig. 8. More synthesized examples of our proposed method are included in Fig. 9. We also show part of the raw natural image samples used in our work in Fig. 10, Fig. 11, and Fig. 12, which helps to evaluate the diversity of the generated data.



Figure 7: **Additional qualitative results from the fine-tuned DDPMs on different domains.** We show qualitative examples for the domain *human faces*, *bedrooms* and *churches* generated from CLIP fine-tuned diffusion models using the same amount of OOD images (1K).



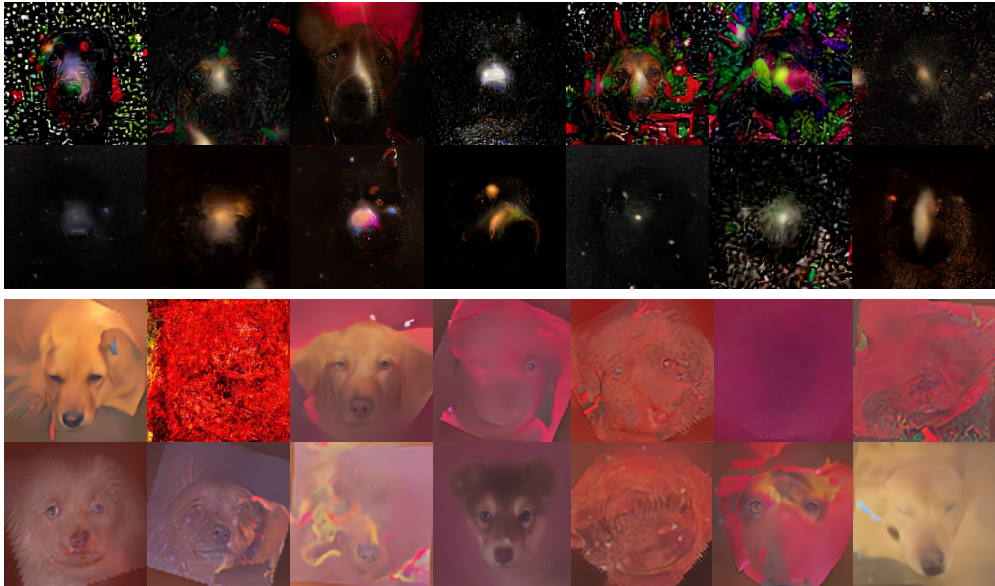


Figure 8: Additional qualitative results from the CLIP fine-tuned DDPMs on the astrophysical data.

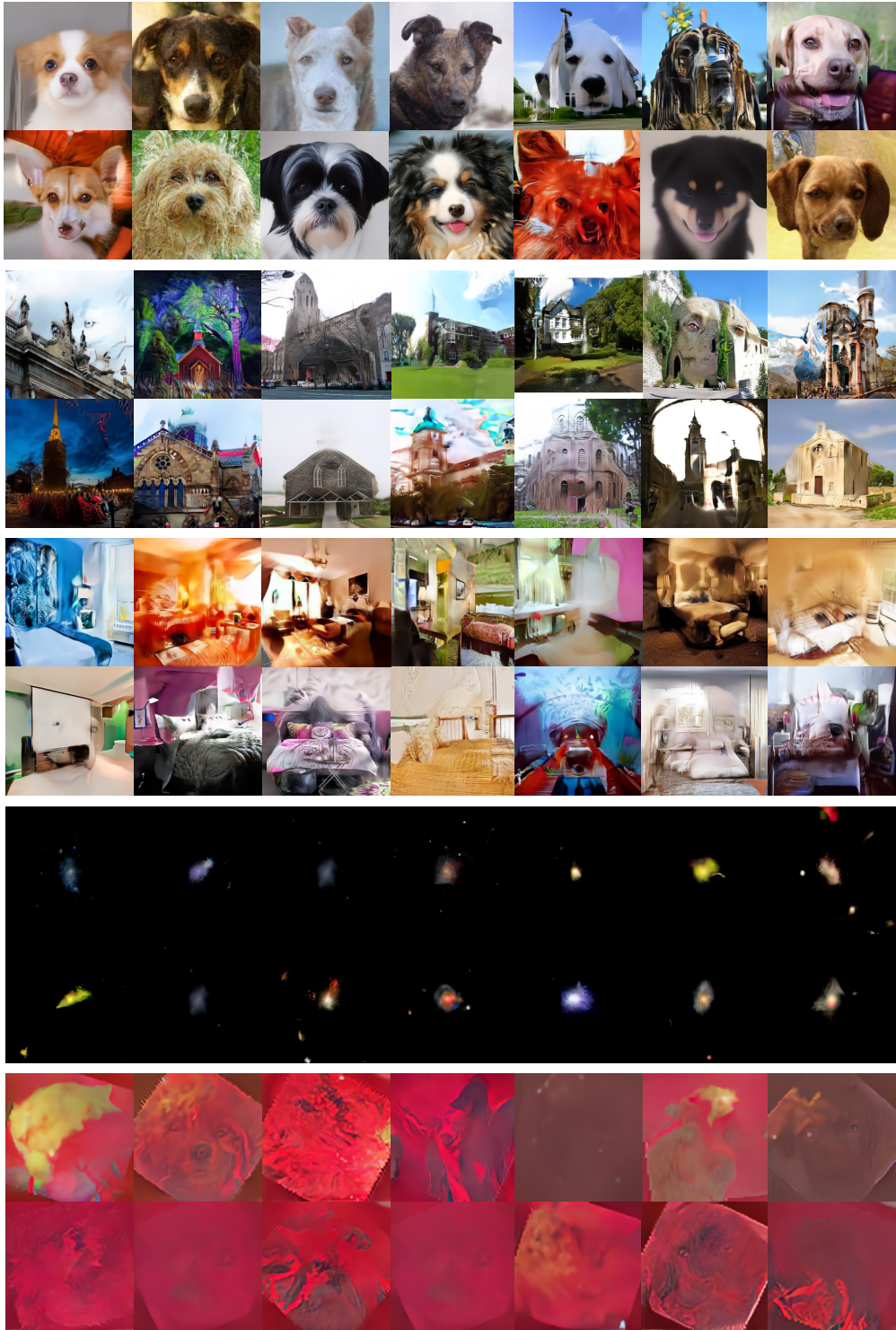


Figure 9: Additional qualitative results from our proposed method for synthesizing OOD data without tuning the model parameters.





Figure 10: Examples of raw human face images used as OOD samples.



Figure 11: Examples of raw church images used as OOD samples.

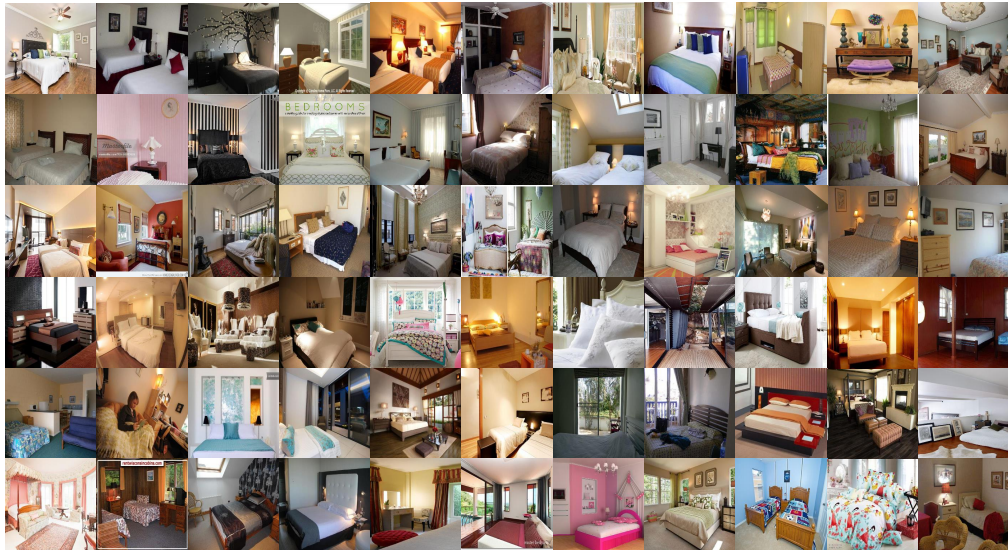


Figure 12: Examples of raw bedroom images used as OOD samples.